A Threshold-Based Bioluminescence Detector With a CMOS-Integrated Photodiode Array in 65 nm for a Multi-Diagnostic Ingestible Capsule

Qijun Liu[®], *Graduate Student Member, IEEE*, Miguel Jimenez[®], *Member, IEEE*, Maria Eugenia Inda, Arslan Riaz[®], *Graduate Student Member, IEEE*, Timur Zirtiloglu, *Graduate Student Member, IEEE*, Anantha P. Chandrakasan[®], *Fellow, IEEE*, Timothy K. Lu, Giovanni Traverso[®], *Member, IEEE*, Phillip Nadeau, *Member, IEEE*, and Rabia Tugce Yazicigil[®], *Member, IEEE*

Abstract—This article presents a highly miniaturized ingestible electronic capsule for biochemical detection via onboard genetically engineered biosensor bacteria. The core integrated circuit (IC) is a threshold-based bioluminescence detector with a CMOS-integrated photodiode array in a 65-nm technology that utilizes a dual-duty-cycling front end to achieve low power consumption. The implemented IC achieved 59-nW active power consumption, 25-fA/count resolution, and a 59-fA minimum detectable signal (MDS) using a calibrated optical source. The IC was then integrated with other system components into a battery-powered wireless ingestible capsule measuring just 6.5 mm thick x 12 mm diameter. We demonstrated successful detection of low-intensity bioluminescent signals from bioengineered bacterial sensors when exposed to the intestinal inflammation biomarker tetrathionate in vitro. Together, the IC and mm-scale smart pill systems demonstrate high sensitivity with low-power multiplexed measurement capability suitable for noninvasive disease diagnosis and monitoring in the gastrointestinal (GI) tract.

Index Terms—Bioluminescence detectors, CMOS-integrated photodiodes, ingestible capsules, threshold-based detection.

I. INTRODUCTION

THE gastrointestinal (GI) tract and its chemical environment are integral to our health. The current gold standard

Manuscript received 20 March 2022; revised 19 June 2022; accepted 27 July 2022. Date of publication 25 August 2022; date of current version 24 February 2023. This article was approved by Associate Editor Nick van Helleputte. This work was supported by the Leona M. and Harry B. Helmsley Charitable Trust under Grant 3239. The work of Qijun Liu and Rabia Tugce Yazicigil was supported in part by the Catalyst Foundation. The work of Miguel Jimenez was supported in part by the Translational Research Institute of Space Health under Cooperative Agreement NNX16AO69A. The work of Maria Engenia Inda was supported in part by the Pew Charitable Trusts under Grant 00030623 and in part by the Catalyst Foundation. The work of Giovanni Traverso was supported in part by the Department of Mechanical Engineering, Massachusetts Institute of Technology (MIT), and in part by the Karl van Tassel (1925) Career Development Professorship, MIT. (Corresponding author: Qijun Liu.)

Qijun Liu, Arslan Riaz, Timur Zirtiloglu, and Rabia Tugce Yazicigil are with the Department of Electrical and Computer Engineering, Boston University, Boston, MA 02215 USA (e-mail: rty@bu.edu).

Miguel Jimenez, Maria Eugenia Inda, Anantha P. Chandrakasan, Timothy K. Lu, and Giovanni Traverso are with the Massachusetts Institute of Technology, Cambridge, MA 02139 USA.

Phillip Nadeau is with Analog Devices Inc., Boston, MA 02110 USA. Color versions of one or more figures in this article are available at https://doi.org/10.1109/JSSC.2022.3197465.

Digital Object Identifier 10.1109/JSSC.2022.3197465

for monitoring the GI tract includes endoscopic biopsies and stool analysis. While these methods are used to diagnose diseases, such as inflammatory bowel disease, they are either invasive (endoscopic biopsies) or lead to the degradation of valuable but labile biomarkers (stool analysis) [1], [2], [3]. Commercial electronic diagnostic pills, such as PillCam and SmartPill, provide a noninvasive and real-time alternative [4]; however, these electronic-only systems cannot directly monitor the gut chemical environment.

Electronic pills with cell-based sensing elements would be ideal for monitoring the GI chemical environment because intestinal microbes naturally survive and sense molecules in the GI tract with high sensitivity and specificity [5], [6]. Cellbased biosensors are also cost-effective because they do not require the laborious purification processes involved in proteinand nucleic acid-based sensing elements [7], [8], [9]. In fact, cell-based biosensors have been demonstrated in a range of point-of-care test (POCT) applications, including medical diagnostics [10], food production [11], and environmental monitoring [12], [13]. Despite this opportunity, there are no commercial examples of an electronic pill that incorporates cell-based biosensors for monitoring the GI tract. A key remaining obstacle is the reduction of the overall system size to prevent GI tract blockage while maintaining adequate bacterial-electronic coupling. Here, we tackle this challenge by implementing a custom integrated circuit (IC) that can quantify an ultra-low light signal from biosensor bacteria on a nanowatt power budget enabling a significant size reduction of all the key components of an integrated bacterial-electronic diagnostic pill.

Electronic-based readout elements complement the sensing features of cell-based biosensors, allowing real-time, wireless communication of the results from inside the body to consumer electronics [14], [15]. However, unlike biosensors based on biomolecule-functionalized electrodes [16], [17], [18], bacteria cannot be as readily coupled to electronics in a small form factor. Bacterial-electronic coupling modalities based on the absorption and/or emission of light are ideal in the harsh aqueous environment of the gut because they allow for complete galvanic isolation of the electronic components. Of these, bioluminescence provides the most

0018-9200 © 2022 IEEE. Personal use is permitted, but republication/redistribution requires IEEE permission. See https://www.ieee.org/publications/rights/index.html for more information.

volume and power-efficient option because, unlike colorimetric (biosynthesis of pigments) [19] or fluorescent (expression of fluorescent proteins) [20], [21], [22] signals, it does not require a light source or optical filters. In addition, the natural human gut environment is dark, allowing a bioluminescent signal to act as a unique marker of the cell-based biosensor. However, even optimized bioluminescent signals from bacteria tend to be very weak (\approx 20–200 photons/sec/cell) [23] and have been traditionally quantified using large, power-hungry bench-top instruments (e.g., plate readers and gel imager). Therefore, an ultra-low-power electronic system capable of acquiring and encoding these weak bioluminescent signals would offer the possibility of distributed and cost-effective POCTs and disease monitoring.

Detection of weak bioluminescent signals could, in principle, be accomplished with known light-to-digital converters that use transimpedance amplifiers [24] or sigma-delta $(\Sigma \Delta)$ analog-to-digital converters (ADCs) [25]. However, these approaches would require a large transimpedance amplifier gain or high ADC resolution leading to high power consumption and hardware design complexity. For example, some μ W- to mW-level systems with integrated photodiodes and an operational transconductance amplifier (OTA)-based readout [26], [27], [28] were able to acquire a weak cell-based luminescent signal. Recently, there was a successful demonstration of an nW-level amplifier system; however, the overall system used off-chip commercial phototransistors (with $100 \times$ intrinsic gain), which resulted in a size that carries a significant risk of intestinal blockage [29], [30]. These systems are either too power-hungry or too large to be safely used as an ingestible diagnostic pill in humans [2]. There is a need to reduce the power consumption to reduce the battery size and, ultimately, the capsule size to improve safety.

An alternative approach is to simply increase the volume and quantity of the bioluminescent sensor bacteria to boost their light signal (e.g., $10\text{--}100~\mu\text{L}$ [30]). However, these solutions limit the miniaturization and the scalability to support multiplex measurements from cell-based biosensors. Therefore, there is an urgent need to develop ICs that can acquire weak bioluminescent signals from <10 μL of cells using a scalable architecture capable of higher multiplexing while consuming nW power levels.

The work presented here demonstrates a wireless ingestible capsule, composed of genetically engineered bacterial biosensors [32] for sensing and ICs for signal encoding and communication, with a total electronic system size of 6.5 mm \times 12 mm, as shown in Fig. 1. The bacterial biosensors produce a light signal that increases over a period of 1–3 h when exposed to disease biomarkers (e.g., tetrathionate) [32]. This occurs through a protein signaling cascade leading to the production of a set of enzymes that result in bioluminescence [32]. A key component of this capsule is a custom-designed thresholdbased bioluminescence detector IC [31] consuming nW-level active power while achieving high sensitivity and high resolution. To achieve this performance, we developed a readout circuit architecture integrating an array of photodiodes in CMOS with low-power luminescent signal processing techniques (i.e., threshold-based encoding). Together, these advances allowed

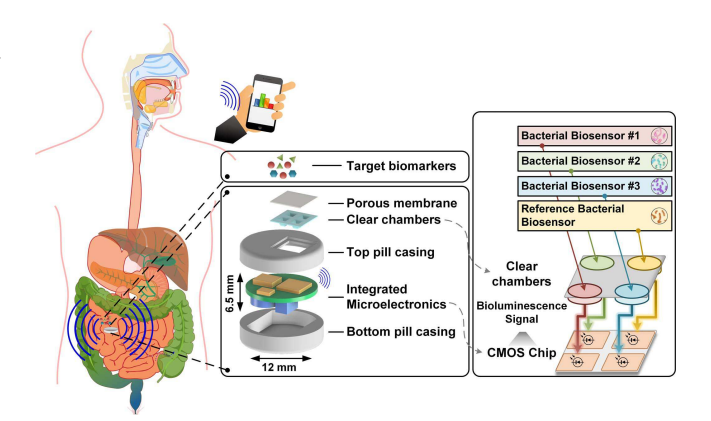


Fig. 1. Ingestible bio-engineered sensor capsule at mm scale detecting target labile biomarkers in the GI tract [31].

detections of fA-level photocurrents from just 1 μL of bacterial cells.

Overall, our power-efficient IC enabled a complete wireless ingestible capsule consuming 16.3 μ W supplied by a small form-factor 5.5-mAh coin-cell battery. In the future, this power level could be alternatively supplied through a battery-less system using biofuel cells [33], [34], [35] since the target lifetime of the system is the time of GI transit (i.e., 8–48 h depending on diet, individual physiology, and disease state [36]).

This article is organized as follows. Section II presents the overall system architecture and key features. Section III discusses the circuit-level implementation and analysis of the threshold-crossing-based bioluminescence detector. The measurement setup and results are presented in Section IV, followed by the conclusions in Section V.

II. MULTI-CHANNEL AND TIME-MULTIPLEXED BIOLUMINESCENCE DETECTOR

The bioluminescence detector shown in Fig. 2 performs luminescence detection from three independent bacterial biosensors via CMOS-integrated photodiodes. A fourth channel is reserved as a reference to calibrate the background light and temperature and channel variations. The bioluminescence detector has three key features: 1) a CMOS-integrated two-by-two photodiode array to provide a scalable biomarker detection platform; 2) a threshold-detection-based bioluminescence processing circuit to achieve high sensitivity and resolution with low energy consumption; and 3) a sleep/wake activation through a dual-duty-cycling front end to lower the average power consumption.

This application-specific IC (ASIC) has four parallel hardware channels consisting of a CMOS-integrated photodiode and a threshold-based bioluminescence encoder embedded in each channel. First, within each chamber, unique bacterial biosensors will bind to their respective target biomarkers causing a light signal to be emitted, which is then converted to a photocurrent by the photodiode. Subsequently, this photocurrent is encoded into threshold-crossing time information, annotated as $(t_{V_{P_i}})$, which is processed by a shared time-to-digital converter to quantify the light level and

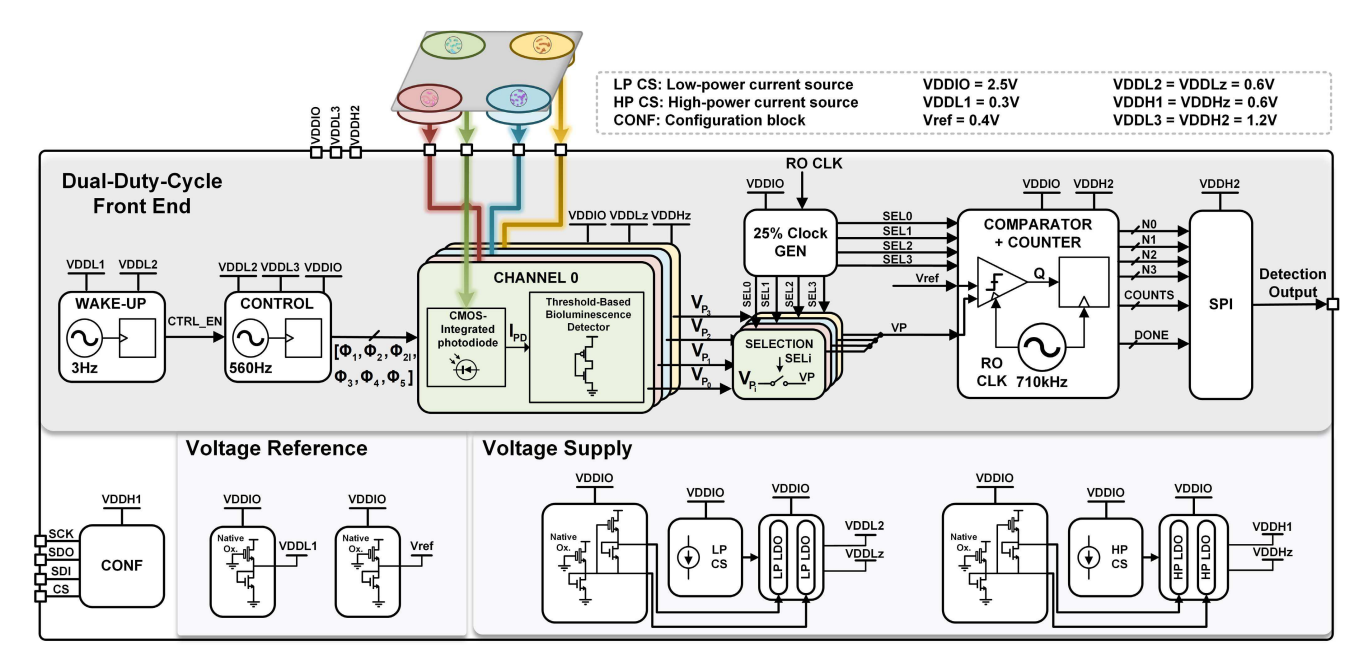


Fig. 2. Threshold-based bioluminescence detector IC with a CMOS-integrated photodiode array and a sleep/wake activation through a dual-duty-cycle front end [31].

output digital counts proportional to the signal strength, hence constructing a detected biomarker level. The time-to-digital converter is composed of a comparator and a counter sharing a ring oscillator. In addition, since the four parallel channel outputs share the time-to-digital converter, timeinterleaved switches, driven by a 25%-duty-cycle clock at 178 kHz, are used to select the active channel. The digital counts from the four hardware channels can be read out through an on-chip digital controller equipped with a serial-toparallel (SPI) interface operating at 160 kHz and 1.2 V. The SPI communicates externally to an onboard microcontroller with a wireless transmitter (PIC12LF1840T39A, Microchip), which then relays the counts wirelessly to a separate base station (CC1200, Texas Instruments) located 1-3 m away. This setup was used for optical characterization and in vitro testing.

Duty cycling is used to reduce the average power consumption. During the first level of duty cycling, a global slow wake-up timer activates the ASIC for bioluminescence detection. The critical biological events occur over a slow transient process, typically minutes to hours; thus, the wakeup timer [37], [38] is designed to support a tunable frequency range of 2–6 Hz for activating the ASIC. When the CTRL_EN signal generated by the wake-up timer becomes high, a shared control block provides clock signals Φ_1 to Φ_5 generated by a gate-leakage-based oscillator [37], [38] operating at 560 Hz and a programmable counter. These specific clock cycles provide the mechanism for encoding the light signal into time information while enabling the second level of duty cycling. Furthermore, the ASIC includes two- and four-transistor voltage references, current references, and lowdropout regulators (LDOs) for supplying different voltage levels for the circuit blocks.

A. Custom Photodiode Design in Standard CMOS Technology

Three main diode types are available for design in standard CMOS processes: n+/p-sub, n-well/p-sub, and p+/n-well/p-sub [39]. The key performance parameters of a CMOS photodetector are responsivity and dark current level. These parameters depend on the process technology, diode type, and diode geometry. The p+/n-well/p-sub diode was selected to implement photodiodes in the proposed architecture primarily due to its high responsivity [39]. Each hardware channel converts the light signal emitted by biosensors to a photocurrent using a single p+/n-well/p-sub photodiode with a dimension of 1.24 mm × 1.24 mm and a sensitive area of 0.9 mm². The array of photodiodes provides simultaneous measurements from three independent biosensors and a reference channel, where each diode is placed at a corner of the chip.

The cross section of a p+/n-well/p-sub photodiode is illustrated in Fig. 3(a). The metal contacts are placed only on the side of the active areas to increase the fill factor. An additional resist-protection-oxide (RPO) layer blocks the silicide diffusion, converting a semiconductor p-n junction diode into a photodiode. A CMOS-integrated photodiode can be represented by an equivalent model consisting of a dc current source I_{PD} in parallel with a shunt resistor (R_{shunt}) and a junction capacitor (C_{PD}) , as shown in Fig. 3(b). The shunt resistance is measured by sweeping a small range of negative to positive voltages, e.g., $V_{PD} = -10$ to 10 mV, across the photodiode and reading out the diode current to back-calculate the resistance. Hence, R_{shunt} is defined as the slope of the current-voltage curve when the bias voltage across the photodiode is close to the origin ($V_{PD} = 0$). The shunt resistance of photodiodes on this chip was measured as ≈ 10 s of $G\Omega$ using

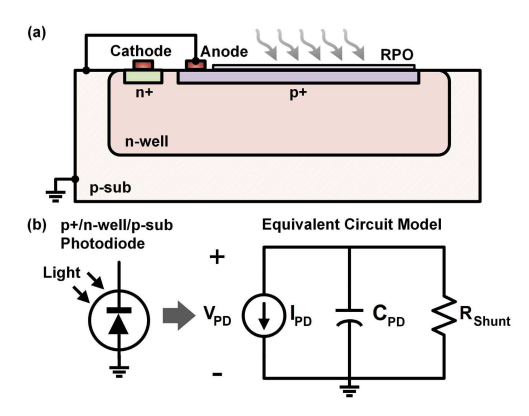


Fig. 3. (a) Cross section of p+/n-well/p-sub photodiode in standard CMOS technology. (b) Equivalent circuit model for the photodiode.

a standalone chip discussed in Section IV-A. Dark current was measured using the same standalone photodiode chip by sweeping a small range of voltages across the photodiode in a dark environment.

The photodiode junction capacitance $C_{\rm PD}$ is proportional to the diffusion area and inversely proportional to the bias voltage across the photodiode ($V_{\rm PD}$). Responsivity is defined as the sensitivity times the junction capacitance, where the sensitivity of a photodiode is defined as the output voltage per unit time divided by the optical input power in V/s·W. The p+/n-well/p-sub type photodiode has two junction capacitances in parallel: 1) p+ to n-well and 2) n-well to p-sub, thus introducing a greater junction capacitance than the other types of p-n junction diodes in the CMOS process. All three types of diodes surveyed in [39] had a similar sensitivity at a large diode area and 490-nm wavelength; therefore, the one with the highest capacitance is expected to have the highest responsivity embedded within it. Hence, higher responsivity is expected by using the p+/n-well/p-sub photodiode [39].

The noise sources of a photodiode can be categorized as thermal noise from the photodiode's shunt resistor ($R_{\rm shunt}$), shot noise from optical power represented by $I_{\rm PH}$, and dark current (I_D) for a noise bandwidth (B), as shown in the following equation:

$$i_n^2 = \left[\frac{4kT}{R_{\text{shunt}}} + 2q(I_D + I_{\text{PH}})\right]B\tag{1}$$

where k is Boltzmann's constant, T is the temperature, and q is the electric charge [40], [41], [42], [43].

Maintaining a near-zero bias voltage across the photodiode allows us to lower the shot noise by minimizing the dark current. At near-0-V biasing, the responsivity of the photodiode is larger than its responsivity in the reverse-biased region. Within the near-0-V region, before the photodiode enters the fully forward bias condition (e.g., when $|V_{\rm PD}| > 10$ mV), the overall photodiode current $I_{\rm PD}$ is approximately equal to the photocurrent generated from an incoming optical signal, e.g., the net light emitted by the bacterial biosensors. Therefore, we reset the bias voltages across the four photodiodes to zero (0 V) for every measurement.

III. CIRCUIT IMPLEMENTATION DETAILS

Here, we discuss the circuit implementation details and key design decisions to achieve scalability, low power, high sensitivity, and resolution for multiplexed bioluminescence measurements via a miniaturized ingestible capsule. Due to the slow-speed operation and low leakage design requirement, analog circuit blocks were implemented using thick-oxide I/O devices. Synthesized digital circuit blocks were implemented using core devices.

A. Threshold-Based Bioluminescence Detector

Previous fully integrated bioluminescence detectors use a CMOS-integrated photodiode followed by a continuous-time operational-transconductance amplifier (OTA)-based integrator with high gain and low noise [27]. However, the continuous-time OTA-based detectors consume mW-level power, e.g., 3 mW [27]. These fully integrated solutions require a large battery limiting the miniaturization of an ingestible capsule. In contrast, the luminescence detector in [29] consumes 26 nW of active power, employing a two-by-two array of commercial phototransistors. However, the use of off-chip commercial phototransistors limits the scalability of the multi-diagnostic system, as this solution is packaged in a large ingestible capsule (3 cm \times 1 cm), which adversely impacts human safety and ease of use.

We designed a threshold-based bioluminescence detector integrating CMOS photodiodes to address the miniaturization challenges while achieving high-sensitivity and high-resolution readout under a tight energy budget. The proposed readout system replaces the power-hungry continuous-time OTA-based integrator in previous fully integrated bioluminescence detectors [27] and fluorescence detectors [20] with a discrete-time front end for low power consumption without sacrificing the integration level and precision. The discrete-time front end consists of a custom dynamic time-threshold-based detection circuit and discharging current source similar to the circuit-level techniques used in zero-crossing-based ADCs [44], [45], [46].

Fig. 4 shows the detailed operation of the threshold-based bioluminescence detector. At the beginning of each measurement cycle, the junction capacitor of each photodiode C_{PD} and capacitors C_1 and C_2 are discharged through switches controlled by clock signals Φ_3 and Φ_4 , as shown in Fig. 4(a).

In the sampling phase illustrated in Fig. 4(b), Φ_1 is designed to be closed for a period (t_{sample}) of 16–26 s, which can be programmed by the control block. The photodiode current I_{PD} , composed of desired photocurrent generated from bioluminescence (I_{PH}) and unwanted dark current (I_D), is integrated on the diode junction capacitor (C_{PD}) over this sampling period (t_{sample}). Negative bias voltage V_{IN} [$V_{\text{IN}} = V_{\text{PD}}$ in Fig. 3(b)] across the photodiode junction capacitor C_{PD} is sampled on the top plate of the capacitor $C_1 = 20~pF$, whereas the bottom plate samples V_{CM} is generated via a two-transistor voltage reference [47] and set to 0.3 V, and it is equal to half VDDHz of the threshold-based detection circuit. This builds up a total charge of $Q_{\text{sample}} = C_1 \cdot (V_{\text{CM}} + \Delta V_{\text{IN}})$. Since V_{IN} is reset to zero by discharging C_{PD} at the beginning of every

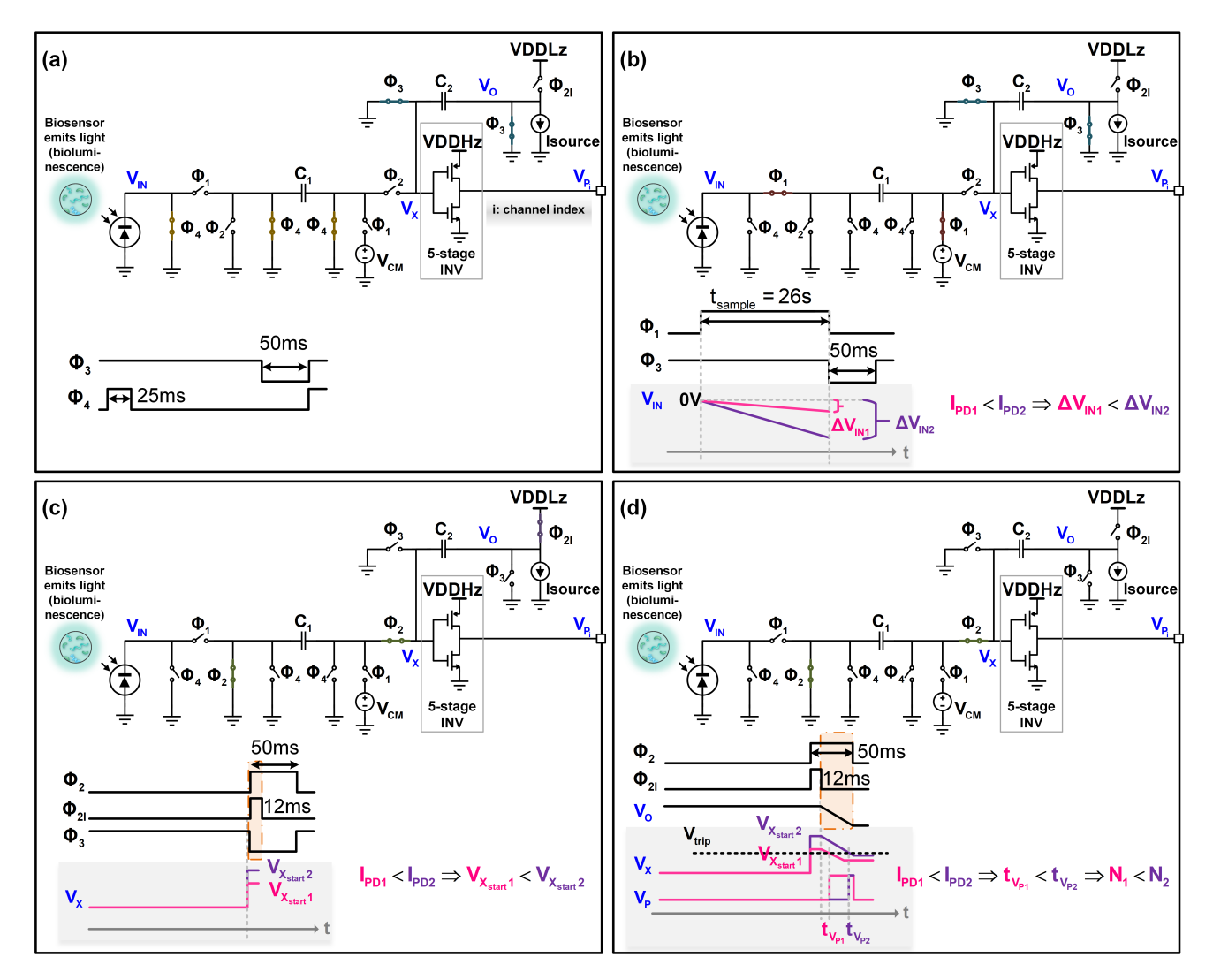


Fig. 4. Operational phases of the threshold-based bioluminescence detector. (a) Reset. (b) Sampling. (c) Charge transfer. (d) Output discharge.

measurement, $\Delta V_{\rm IN}$ is given by

$$\Delta V_{\rm IN} = 0 - V_{\rm IN} = |V_{\rm IN}| = \frac{I_{\rm PD} t_{\rm sample}}{C_{\rm PD}}.$$
 (2)

The dark current is minimized when applied bias across the photodiode is near zero to ensure a linearly proportional relationship between the photodiode current (I_{PD}) and the optical power of bioluminescence produced by the bacterial cells. In our design, we reset the bias voltage across the photodiode at the beginning of each measurement cycle and set the sampling period duration (t_{sample}) such that the maximum bias voltage across the photodiode does not exceed 10 mV.

During the charge-transfer phase shown in Fig. 4(c), Φ_{2I} is active for a short period, ≈3 ms to 12 ms, concurrently with Φ_2 , $\approx 12-50$ ms, to reset V_O node to the VDDLz voltage of the threshold-based detector block, VDDLz = VDDHz = 0.6 V. The active period of Φ_2 is configured through the programmable counter, as discussed in Section III-B. The active period of Φ_{2I} is equal to (1/4) of the active period of Φ_2 . The expected maximum photocurrent, SPI and transmitter frequency, and the communication delay between on-chip and

off-chip components set the optimum value of Φ_2 active time. The charge built up during the sampling phase is transferred to $C_2 = 5$ pF, setting V_X node to a voltage level that is linearly proportional to bias voltage across the photodiode $V_{\rm IN}$ during the Φ_{2I} active period

$$Q_{\text{transfer}} = C_1 \cdot V_X + C_2 \cdot (V_X - \text{VDDLz}) \tag{3}$$

$$Q_{\text{sample}} = Q_{\text{transfer}}$$
 (4)

$$Q_{\text{sample}} = Q_{\text{transfer}}$$

$$V_{X_{\text{start}}} = \frac{(V_{\text{CM}} + \Delta V_{\text{IN}}) \cdot C_1 + \text{VDDLz} \cdot C_2}{C_1 + C_2}.$$
(5)

The threshold-based bioluminescence detector enters an output discharge phase once Φ_{2I} is inactive, as shown in Fig. 4(d). Unlike traditional zero-crossing-based ADCs that sample the output voltage at the V_O node to obtain digital bits [44], the proposed architecture uses the V_O node as a discharging node to drive V_X . This design converts the threshold-crossing time of the V_X node to digital counts. V_X discharges by a programmable six-branch pseudo current source (I_{source}) enabled by Φ_2 , as shown in Fig. 5, at the rate of I_{source}/C_1 . Each parallel hardware channel contains an

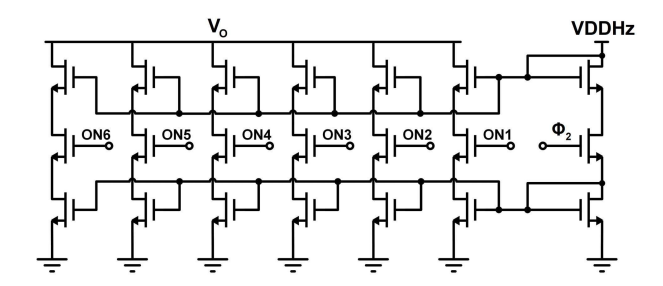


Fig. 5. Programmable discharging current source implementation.

independent current source. The current level, 160–960 pA at 37 °C, is configured through ON1–ON6 static digital bits set by the digital configuration (CONF) block based on the system requirements detailed in Section IV.

As illustrated in Fig. 4, stronger optical power from bacterial biosensors yields a larger input bias voltage across the photodiode (if $I_{\rm PD1} < I_{\rm PD2}$, then $\Delta V_{\rm IN1} < \Delta V_{\rm IN2}$), resulting in a higher starting voltage at the V_X node ($V_{\rm X_{start1}} < V_{\rm X_{start2}}$). Given different initial voltages of V_X , the crossing times ($t_{V_{P_i}}$) of the five-stage inverters' threshold ($V_{\rm trip}$) will linearly vary with $I_{\rm PD}$ and, hence, $\Delta V_{\rm IN}$. A higher $V_{\rm X_{start}}$ voltage requires a longer time to cross the inverters' threshold $V_{\rm trip}$, which is set at 300 mV for this work. The threshold-crossing time ($t_{V_{P_i}}$) is back-calculated from count values, N, reported by the SPI at 160 kHz. $t_{V_{P_i}}$ depends on the discharging rate ($I_{\rm source}/C_1$), initial voltages of V_X , and the inverters' threshold voltage ($V_{\rm trip}$). The resolution of the threshold-based bioluminescence detector is defined as

Resolution =
$$\frac{\Delta I_{\text{PD}}}{\Delta t_{V_{P_i}}}$$

= $\frac{\Delta I_{\text{PD}}I_{\text{source}}}{C_1\Delta V_X} = \frac{\Delta I_{\text{PD}}I_{\text{source}}}{C_1\Delta (V_{X_{\text{start}}} - V_{\text{trip}})}$
= $\frac{\Delta I_{\text{PD}}I_{\text{source}}}{C_1\Delta V_{X_{\text{start}}}}$. (6)

B. Wake-Up Timer and Control Clock Generator

In this system, gate-leakage-based three-phase oscillators [37], [38] achieving low energy per cycle are chosen for generating the slow wake-up timer and low-frequency control clocks for the detector. As shown in Fig. 6(a), a gate leakage transistor M_{7w} provides a small reference current (60 fA) to discharge the capacitor network (C_0, C_1, C_2) until the threshold voltage of M_{5w} is reached. A strong turn-on of M_{5w} flips the voltage across capacitor C_3 , hence inverter's input [INV1 in Fig. 6(a)], with the help of feedback transistor M_{3w} . Each of these dynamic delay stages is connected in series to form a low-energy three-stage relaxation oscillator, as shown in Fig. 6. A low-power two-transistor voltage reference [47] generates a stable voltage reference of VDDL1 = 0.3 V from the main supply to support the wake-up oscillator operation in both active and sleep modes. The wake-up oscillator is tunable through configuration bits VC1 and VC2 to obtain a slow clock with a nominal frequency of 3 Hz and achieves a measured temperature coefficient of 1.3% per degree with a simulated

energy consumption of 1.63 pJ/cycle. A programmable digital wake-up counter using the output from the wake-up oscillator generates an enable signal CTRL_EN to activate the remaining analog front-end blocks, which forms the first level of duty cycling, as shown in Fig. 6(c).

The second programmable counter uses a 560-Hz clock generated by a gate-leakage-based three-phase oscillator, as shown in Fig. 6(b), with no tuning capacitors. This counter generates several switch-control signals, $\Phi 1-\Phi 5$, as shown in Fig. 6(c). $\Phi 1$ ranges from 16 to 26 s to avoid fully forward biasing of the photodiode. The control oscillator achieves a measured temperature coefficient of 10% per degree with a simulated energy consumption of 342 fJ/cycle. These gate-leakage-based oscillators offer significantly low energy consumption per cycle at the expense of degraded temperature stability performance. Since our application of interest is an ingestible capsule for disease diagnosis and monitoring, the temperature is stable at ≈ 37 °C for nominal body temperature. Given the low energy consumption of the gate-leakage-based oscillators, both wake-up and control oscillators are continuously running.

C. Time-to-Digital Converter

The output of each threshold-based bioluminescence detector channel is a step voltage (V_{P_i}) from 0 to VDDHz = 0.6 V. An analog multiplexer is designed for the time-interleaving of the four parallel channels. These time-interleaved switches are driven by a 25% duty-cycle clock generator to select the active channel output V_{P_i} for digital processing. The analog multiplexer output, VP signal, is fed to a StrongArm-latch comparator [48], as shown in Fig. 7(a), clocked by a current-starved ring oscillator [49], [50] with a measured frequency of 710 kHz. The VP voltage is compared to a voltage of $V_{\rm ref} = 0.4$ V provided by a two-transistor voltage reference.

As shown in Fig. 7(b), the current through M_{1p} and M_{1n} of five-stage inverter-based RO is constrained by the current mirror formed by $M_{1r}-M_{3r}$ to M_{2p} and M_{2n} . The current flowing through the inverter chain can be adjusted via a tunable I_{ref} that is current mirrored from a high-power on-chip current source (HP CS), as discussed in Section III-D.

The 25% duty-cycle clock generator, as shown in Fig. 7(c), clocked by the current-starved RO, is composed of two-stage divide-by-2 circuits and buffers/inverters to obtain delayed clocks (Id and Qd) and inverted clocks (I- and Q-) at 1/4 of the RO clock frequency. These signals, Id, I-, Qd, and Q-, are provided to AND gates for obtaining 25% duty-cycle channel selection signals, SEL0–SEL3. As shown in Fig. 7(a), initially, when RO clock is low, both M_1 and M_2 are OFF. Once RO clock goes high, S_1 – S_7 turn off, and transistors M_1 and M_2 are ON, drawing a differential current in proportion to VP and V_{ref} and discharging drain voltages on M_1 and M_2 . If VP is greater than V_{ref} , the discharging on M_1 happens quicker compared to M_2 and crosses the threshold voltage of M_3 earlier. M_3 turns on, allowing discharging current to flow through M_6 and creating a rising edge of the comparator output (Q). A synthesized digital counter, Q counter, takes RO clock, selection signals (SEL 0-SEL 3), and comparator output (Q) as inputs. At each falling edge of the RO clock, the Q counter reads all selection signals (SEL0-SEL3). SEL0

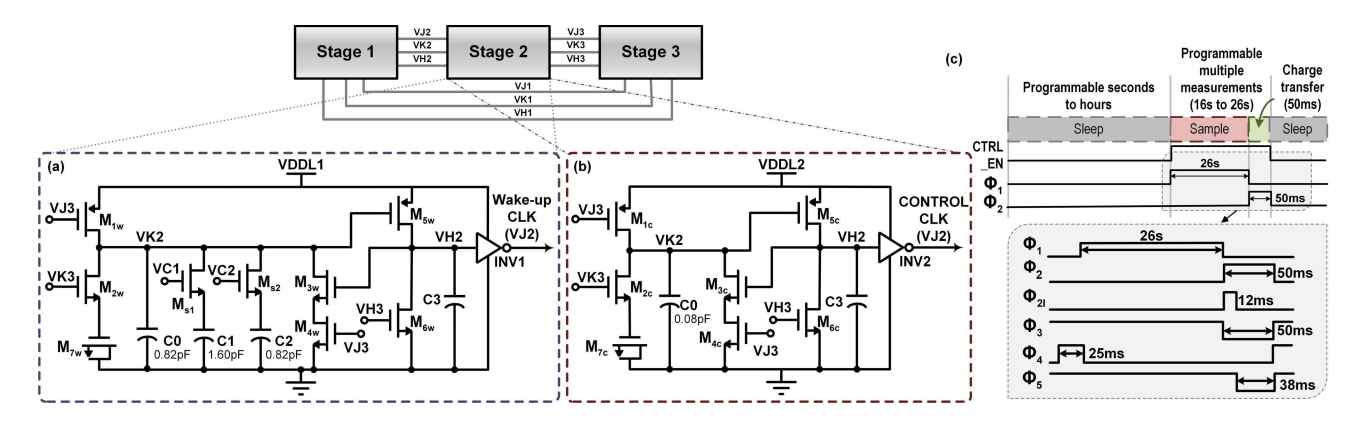


Fig. 6. Gate-leakage-based three-phase oscillators: (a) wake-up oscillator and (b) control oscillator. (c) Dual-duty-cycling timing diagram of the threshold-based bioluminescence detector.

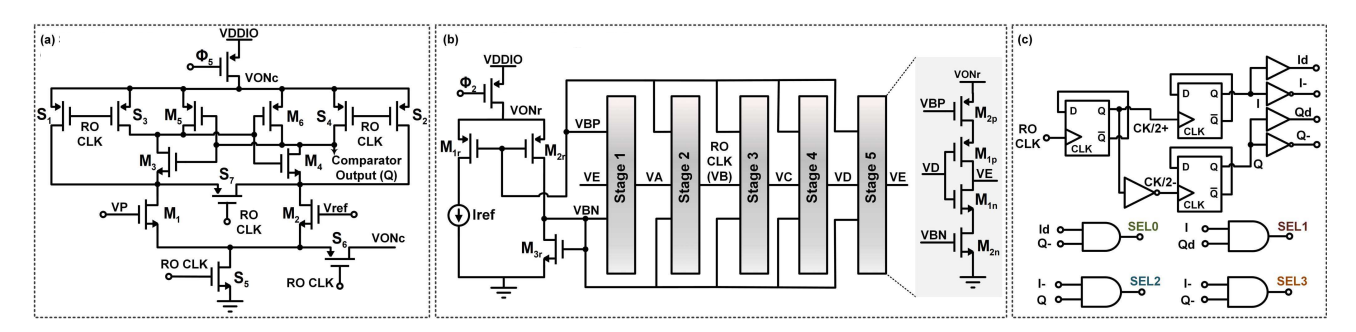


Fig. 7. Circuit blocks of the time-to-digital converter: (a) StrongArm-latch dynamic comparator, (b) current-starved ring oscillator, and (c) 25% duty-cycle clock generator.

being high indicates that the comparator outputs a decision for channel 0. In the meantime, the Q counter keeps track of the number of RO clock cycles until each channel observes its first rising edge of the comparator output. Fig. 8 illustrates the input and output signals of the time-to-digital converter for the example scenario. Given that photocurrent I_{PD1} is smaller than I_{PD2} for channel 0, the crossing time of the inverters' threshold (V_{trip}) due to I_{PD1} is shorter than the crossing time of the threshold (V_{trip}) due to I_{PD2} ; hence, V_{P_1} switches from low to high earlier than V_{P_2} in Fig. 8. The Q counter observes the first comparator output high at the second SEL0 pulse for V_{P_1} , while V_{P_2} is high during the third SEL0 pulse. Consequently, the Q counter outputs a smaller N_1 compared to N_2 in this example scenario. The threshold-crossing time of each channel and resolution based on the number of digital counts and the clock period of the ring oscillator can be defined as

Resolution =
$$\frac{\Delta I_{\text{PD}}}{\Delta t_{V_{P_i}}} = \frac{\Delta I_{\text{PD}}}{\Delta N_i \times T_{\text{RO}}}$$
 (7)

where ΔI_{PD} is the difference between photocurrents, e.g., I_{PD1} and I_{PD2} , corresponding to different bioluminescence levels, $\Delta t_{V_{P_i}}$ is defined as the difference between the threshold-crossing times for two different photocurrent levels, ΔN_i is the difference between N_1 and N_2 , as shown in Fig. 8, and T_{RO} is the period of the current-starved ring oscillator clock.

The current-starved ring oscillator and the 25% duty-cycle clock generator are activated only when Φ_2 (12–50 ms) is

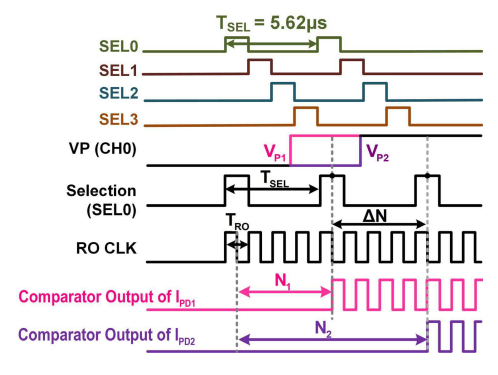


Fig. 8. Time-to-digital converter input and output signal waveforms for an example detection scenario when the photocurrent I_{PD1} is smaller than I_{PD2} for channel 0.

high, while the dynamic StrongArm-latch-based comparator and the digital Q counter are activated when Φ_5 (9–38 ms) is low. This second level of the dual-duty-cycling scheme allows us to minimize the average power consumption of the higher frequency circuits.

D. Power Management Unit

The power management unit consisting of two on-chip LDO/current reference pairs provides stable supply voltages at 0.6 V to different circuit blocks by drawing current off the main supply of the ingestible capsule, a coin-cell battery (5.5 mAh) providing 2.5–3 V. The first pair, LP CS and LP LDO, is designed to operate at low average current

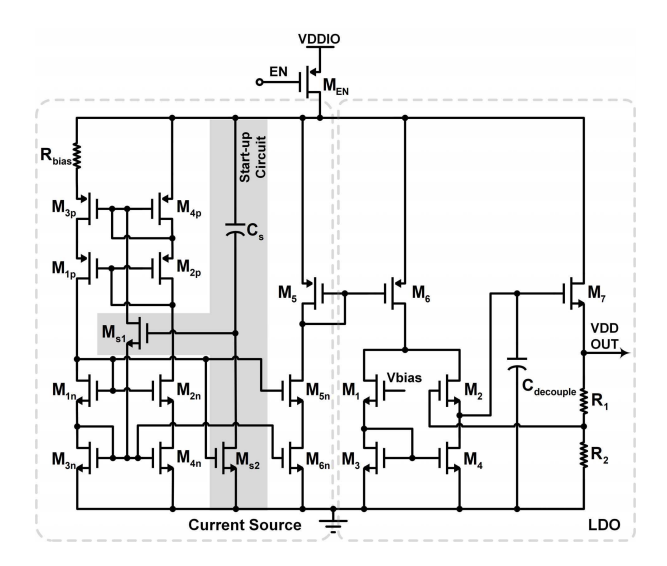


Fig. 9. Architecture of on-chip current source and LDOs providing stable supply voltages of 0.6 V for various circuit blocks of the multi-channel and time-multiplexed bioluminescence detector chip.

levels (\approx 7 nA) for supplying the low-power oscillators, level shifters, and the reset of the V_O node of the threshold-based bioluminescence detectors. The second pair, HP CS and HP LDO, is designed to operate at a higher average current level (\approx 0.6 μ A) to support power-hungry digital controllers.

Both HP and LP LDOs with their current sources have similar architectures, as shown in Fig. 9 [51]. The proportional-to-absolute-temperature (PTAT) current reference with a startup circuit, formed by C_s , M_{s1} , and M_{s2} , leverages the bias resistor $R_{\rm bias}$ value to set the average current levels and provide a reference current for the LDO. The on-chip LDO consists of a power transistor (M_7) and a single-stage differential error amplifier. The positive error amplifier input monitors the fraction of the LDO output set by the resistor ratio of R_1 and R_2 , while the negative error amplifier input is connected to a stable bias voltage, $V_{\rm bias}$, generated by a four-transistor voltage reference [47].

IV. MEASUREMENTS

The chip was fabricated in 65-nm CMOS technology. Fig. 10(a) shows the chip micrograph and the printed circuit boards (PCBs) hosting the ingestible multi-diagnostic capsule system in an mm-scale form factor. The upper side of the top PCB holds the quartz-lid QFN-packaged custom-designed CMOS multi-channel and time-multiplexed bioluminescence detector. A 6.8 mm × 2.1 mm coin-cell battery (MS621FE, Seiko Instruments) provides the main supply voltage for all of the components on the PCB. The commercial wireless microcontroller and transmitter IC with its matching network that connects to an antenna (0915AT43A0026, Johanson Technology) are located on the bottom PCB, as shown in Fig. 10(b). The microcontroller writes the configuration bits into the custom CMOS bioluminescence chip's digital controller block. Once the microcontroller detects an interrupt signal [Done signal in Fig. 10(b)] from the bioluminescence chip indicating threshold crossing of all four sensing channels,

the microcontroller requests the digital counts corresponding to the threshold-crossing time of the bioluminescence detector from the on-chip SPI. The wireless transmitter IC communicates out of the body to a commercial receiver (CC1200, Texas Instruments). Each wireless packet is 232 bits long with a preamble/header and is transmitted at 40 kb/s with +10-dBm power, resulting in a wireless transmission for 5.8 ms at 915 MHz using a frequency-shift-keying (FSK) modulation.

In the following, we first show the optical measurements of the ingestible capsule chip. Second, we demonstrate the *in vitro* performance of the bio-engineered system with the genetically engineered bacterial sensors. We conclude this section with a performance comparison against the state-of-the-art implementations.

A. Optical Measurements

We performed preliminary characterization of the genetically engineered bacterial sensors using a standalone p+/n-well/p-sub photodiode chip fabricated in 65-nm CMOS technology without additional readout circuits. This standalone chip includes a photodiode with the same size and physical structure as the photodiodes of the custom CMOS bioluminescence detector. The standalone chip was connected to a sub-femtoamp source measurement instrument (K6430, Keithley Instruments) with 0 V across the photodiode. To measure the maximum expected light signal from the biosensors, 2 μ L of cells contained in an open plastic well with an optically clear thin film bottom (0.1 mm thick) were placed onto the photodiode. The characterization shows that the genetically engineered biosensors yield very low-level optical signals with a maximum of 270 fA. As shown in (6), the resolution value is linearly proportional to the discharging current I_{source} . Therefore, only one branch of the discharging current source was enabled to ensure the best resolution, which represents a lower resolution value, for the ingestible capsule.

The wireless ingestible capsule, the standalone photodiode IC, and an optical meter (PM100D, ThorLabs) were placed inside a metal box to avoid electromagnetic interference on the sub-femtoamp source measurement instrument cable (<0.5 m) used for this special calibration mode, as shown in Fig. 11(a). In addition, the box was covered with a blackout cloth to avoid ambient light from the environment during the optical characterization. The temperature was set to 37 °C by placing the metal box inside a temperature-controlled incubator similar to all biological measurements. Five different voltage levels (0, 2.1, 2.14, 2.165, and 2.185 V) were supplied across a teal LED ($\lambda = 520$ nm) placed 30 cm opposite to both ICs and the optical meter. Different supply voltage levels across the LED yielded different optical power levels, simulating different luminescence levels. The ingestible capsule continuously measured and transmitted a packet wirelessly every 26 s (i.e., the sampling period was set to 26 s) to the receiver. In total, 100 readout packets were transmitted at each LED bias voltage level. At the same time, both the optical meter and the standalone photodiode reported the corresponding optical power level and photocurrent level for this given LED bias voltage. The optical meter with a sensor size of 0.7088 cm² was placed equidistant, 1.5 cm, from the

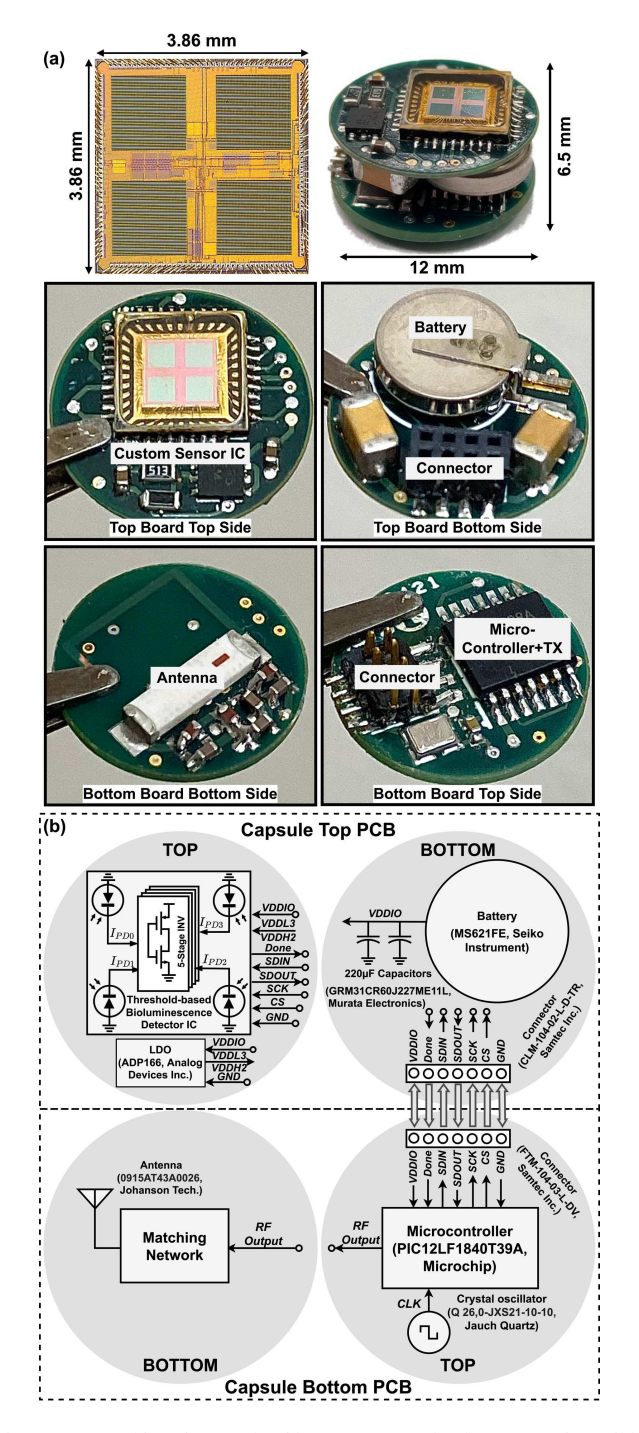


Fig. 10. (a) Chip micrograph (65-nm CMOS technology) [31], ingestible capsule PCB, and system components. (b) Complete system diagram of the ingestible capsule PCB.

ingestible capsule and the standalone photodiode IC, as shown in Fig. 11(a). The sub-femtoamp source meter reported the real-time photocurrent outputted from the standalone photodiode IC. The ingestible capsule IC's second channel (CH 2) was covered by a black masking tape, serving as a reference channel for calibration. When the supply voltage across the LED was 0 V, i.e., no light in the metal box, the ingestible capsule readout from each channel was utilized for one-time

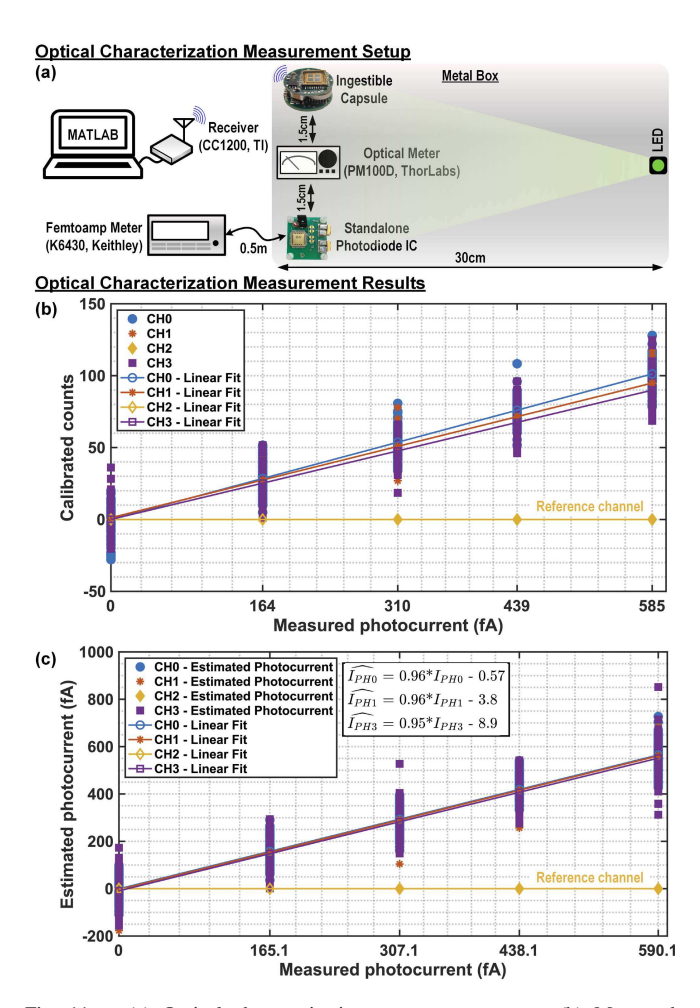


Fig. 11. (a) Optical characterization measurement setup. (b) Measured training dataset to obtain the resolution and the MDS for each hardware channel. (c) Measured test dataset verifying the accuracy of the photocurrent estimation from the training optical characterization.

calibration of the digital-count offset due to fabrication and dark current variations in each channel.

To characterize and obtain the measured minimum detectable signal (MDS) and resolution, we collected training and test data. First, the training optical-characterization dataset was measured by sweeping the five LED bias voltages in a light- and temperature-controlled environment. The resolution of each channel was obtained via measuring the quantities, as defined in (7). ΔN_i is the difference between the luminescence detector IC output counts for two LED bias voltages, and ΔI_{PD} is the difference between photocurrent values reported from the standalone photodiode IC for the same two bias voltage settings. As shown in Fig. 11(b), the individual channel resolution is calculated as the inverse of the slope of the first-order polynomial curve fitting from the measured 500 calibrated digital counts of the luminescence detector IC (y-axis) versus measured photocurrents outputted by the standalone photodiode IC (x-axis). The measured resolution values range from 4.11 to 4.62 fA/ μ s. The MDS is calculated using the average resolution of each channel times 1σ standard deviation of the calibrated digital counts at a given LED bias voltage. The worst case MDS among the four parallel channels

is 71 fA with an average MDS of 59 fA. Second, a test opticalcharacterization dataset was measured the next day using the same experimental setting as the training dataset and used to verify the accuracy of the photocurrent estimation from the training optical characterization. The x-axis data of Fig. 11(c) $(I_{\rm PH})$ are provided by the testing data measured from the standalone photodiode IC, and the y-axis data are provided by the estimated photocurrent (I_{PH}) , which is calculated by multiplying the measured digital counts from the testing dataset with the resolutions obtained from the training dataset. Note that the training data provide the non-dimensionalization of the number of digital counts from the capsule to report consistent photocurrent levels across multiple experiments. A moving window averaging can be applied later to the calibrated counts due to a long biological time constant, and this reduces the noise. Equations denoted in Fig. 11(c) show the linear fit curves of I_{PH} for individual sensing channels. Given that the slopes of the linear-fit curves for all sensing channels are close to 1 with less than 5% offsets, these optical measurements validate a one-time optical calibration procedure, and hence, the substitution of resolutions from the optical calibration is valid for the *in vitro* biological measurements.

B. In Vitro Biological Measurements

After completing the offset calibration and optical characterization of the bioluminescence detector IC, we conducted *in vitro* measurements of the wireless ingestible capsule interfacing with the genetically engineered bacterial sensors. The bioluminescence detector chip was hermetically sealed under a quartz lid and was enclosed by bacterial chambers allowing the maximum light transmission to the CMOS-integrated photodiode array. For the *in vitro* measurements, the wireless ingestible capsule was coated with 2 μ m of Parylene C to act as a moisture barrier. Parylene C coating was performed using Specialty Coating System Labcoter 2 (PDS 2010) following the same protocol described by [30]. The custom-designed 3-D-printed casing encapsulated the coated capsule. Finally, we sealed the casing with Elite Double 22 (Zhermack Dental) to further reduce the chance of leakage.

For the in vitro experiments, overnight cultures were diluted 1:10 in LB (Luria-Bertani) liquid medium, then subcultured for 20 min, and, finally, concentrated 100× by centrifugation. 1–1.5 μ L of the concentrated bacterial cells were added to the bacterial chambers that are placed on top of Channel 0 (CH0) and Channel 3 (CH3), which served as two independent replicate tetrathionate sensing channels. 1–1.5-μL Wild-type bacterial sensor processed the same way as the bacterial cells were added to Channel 1's (CH1) bacterial chamber, which served as a null sensor control with no bioluminescence production. Channel 2 (CH2) also served as an additional reference channel (without bacteria) to calibrate offsets due to channel and temperature variations. Before initiating the in vitro measurements, both LB media and the capsule chip were pre-warmed to 37 °C in the incubator for at least 10 min. The ingestible capsule and LB media were first placed into a beaker, followed by adding an intestinal inflammation biomarker (100-mM tetrathionate). At this point, we started the measurements. The capsule wirelessly transmitted data to a



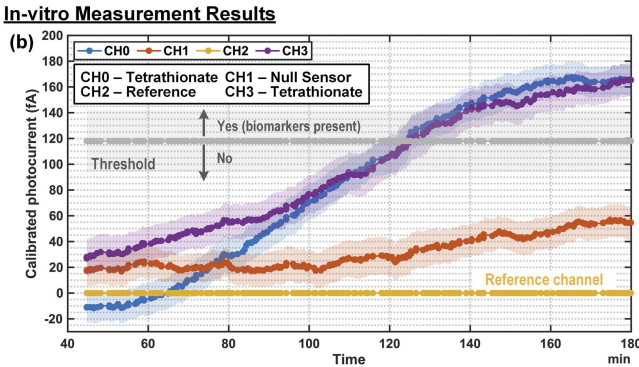


Fig. 12. (a) *In vitro* measurement setup and (b) results indicating the successful detection of bioluminescent signals emitted from the tetrathionate bacterial sensor cells (blue and purple curves) compared to the null sensor with no bioluminescence production (orange curve).

receiver (CC1200, Texas Instruments) over the duration of the experiment for 3 h. After 3 h of exposure to tetrathionate, both CH0 and CH3 detected the bioluminescence illuminated from the exposed tetrathionate sensor cells and reported a maximum 180-fA calibrated photocurrent, while CH1 provided a negative channel set by the system noise, as shown in Fig. 12(b).

Since the ingestible capsule system is designed as a binary classifier in a diagnostic setting, we set the decision threshold to at least $2 \times$ MDS obtained in Section IV-A. Therefore, one could conclude from Fig. 12(b) that the system successfully detected the presence of tetrathionate since the photocurrent signals reported by CH0 and CH3 were significantly higher than the null sensor signal of CH1 and above the binary classifier's decision threshold. The shaded error bars denote the 95% confidence interval for samples over a 45-min sliding window.

C. Performance Summary and Comparison

Fig. 13 summarizes the presented system performance and compares it against the state-of-the-art demonstrations. The results of the multi-channel and time-multiplexed bioluminescence detector IC consisting of a two-by-two array of CMOS-integrated photodiodes demonstrate 5.4× lower MDS and 2.1× higher resolution compared to the first state-of-theart solution [29] at body temperature (37 °C). Furthermore, this chip consumes 59 nW of average active power while providing a multiplexed measurement capability and 50 847× lower average active power compared to the second stateof-the-art solution [27]. Fig. 14 shows the average current consumption of the wireless ingestible capsule system, where the off-chip commercial components' (an RF transmitter, a microcontroller, and an LDO) consumption dominates the total system power consumption. For a future optimized wireless system, one could envision that the transmitter power

Specification	This work	ISSCC '17 [29]	TCAS-1 '07 [27]	VLSI '20 [22]
Detector Type	Bioluminescence	Bioluminescence	Bioluminescence	Fluorescence
Technology (nm)	65	65	350	65
VDD (V)	2.5	2.5	3.3	1.55
Area (mm²)	3.91 ⁽¹⁾ / 0.31 ⁽²⁾	0.76 ⁽²⁾	2.25	4
Capsule Size	6.5 x 12 mm	~ 3 x 1 cm	N.A.	0.9 x 2.4 cm
Photodetector	CMOS-Integrated	Commercial NPN	CMOS-Integrated	CMOS-Integrated
	P+/NWELL/PSUB	phototransistor	NWELL/PSUB	NWELL/PWELL(3)
Multiplexed Biosensing	Yes (2x2 array)	Yes (2x2 array)	No (Single)	Yes (15 pixels)
Sensor IC Average Active Power (nW)	59 ⁽⁴⁾	26	3,000,000	14,000
Capsule Power (µW)	16.3	12.7	N.A.	1,400 ⁽⁵⁾
Integration Time (min)	0.43	0.29	1.47	N.R.
Resolution (fA/count)	25 ⁽⁶⁾	53	N.R.	N.R.
Minimum Detectable Signal (fA)	59 / 71 ⁽⁷⁾	380 ⁽⁸⁾	0.3	N.R.

- (1) Active area including the 2x2 photodetector array (2) Active area.
- (4) Electrical characterization power on a test board with Φ_1 = 16s and Φ_2 = 12ms [31]
- (4) Electrical characterization power on a test locard with $\Phi_1 = 1$ bs and $\Phi_2 = 1$ zm (5) Total power consumption of the chip in the transmitter mode. (6) Average channel ($T_{charmol} = T_{SEL} = 5.82 \mu s$) resolution for I_{PO} range of 0 586fA (7) Worst-case MDS is 71fA and the average MDS is 59fA. (8) Photocurrent for SNR = 0dB N.A. = Not applicable N.R. = Not reported

Fig. 13. Performance summary and comparison with the state-of-the-art bioluminescence and fluorescence detector ICs.

Current Consumption (37°C)					
System (excluding wireless)(1)	2.64μΑ				
Wireless	Calculated	Measured			
Active wireless curent ⁽²⁾	16.5mA				
Packet bits	232 bits				
Bit rate	40kbps				
Packet time	5.8ms				
Sampling interval	26.05s				
Duty cycle	2.23E-04				
Average wireless current	3.58µA	3.88µA			
Total average current	6.22µA	6.52µA			

(1) Measured system power includes a commercial microcontroller (PIC12LF1840T39A, Microchip) and LDO (ADP166, Analog Devices Inc.). (2) Active wireless current is obtained from the

Fig. 14. Average current consumption of the wireless ingestible capsule system at 37°.

will be approximately 138 nW for 232 bit per 26 s based on [52] using a crystal-less Medical Implant Communication System (MICS) TX consuming 15.5 nJ/bit at 200 kb/s. Finally, we demonstrate a significantly smaller form factor (6.5 mm \times 12 mm ingestible capsule) than the state-of-the-art cm-scale wireless ingestible capsules [22], [30].

V. CONCLUSION

The threshold-based bioluminescence detector IC exhibits a dual-duty-cycling front end with a two-by-two CMOS-integrated photodiode array achieving high sensitivity and high resolution while consuming 59 nW of active power. This work demonstrates the first bacterial-electronic ingestible capsule at the mm scale using the integrated CMOS threshold-based bioluminescence detector for simultaneous detection of different labile biomarkers. This system provides a scalable detection platform agnostic to the biomarker of interest, which can serve as a minimally invasive tool for disease diagnosis and monitoring in the GI tract.

APPENDIX MEASUREMENT CALIBRATION

Here, we describe the measurement calibration procedure. One channel acts as a reference channel to cancel any variation between each measurement cycle, while the remaining three channels are used for independent biomarker detection. This calibration scheme is performed for optical and in vitro measurements to obtain calibrated readout output counts. The threshold-based bioluminescence detector output counts of the

three sensor channels are denoted as N_i : $i = \{0, 1, 2\}$. The number of counts required for crossing the threshold is given

$$N_i = \frac{\Delta t_{V_{P_i},i}}{T_{RO}} = \frac{C_{1,i}(V_{X_{\text{start}},i} - V_{\text{trip},i})}{T_{RO}I_{\text{source},i}}.$$
 (8)

Given (2) and (5), N_i is composed of two parts: 1) output counts due to circuit-design parameters (e.g., terms in (9) related to common-mode voltage $V_{\rm CM}$ and VDDLz) and 2) output counts due to photocurrent generated from the incoming light signal (bioluminescence). Ideally, the first part of (9), $N_{i,CM}$, is the same for all channels when there are no channel variations. We introduce a temperature-dependent scaling function, f(T), in each cycle. S_i is a scaling constant that depends on the circuit-design parameters

$$N_{i} = \left(\frac{C_{1,i}^{2} V_{\text{CM},i} + \text{VDDLz} \cdot C_{1,i} C_{2,i} - V_{\text{trip},i} (C_{1,i} + C_{2,i}) C_{1,i}}{(C_{1,i} + C_{2,i}) I_{\text{source},i} T_{\text{RO}}} + \frac{C_{1,i}^{2} I_{D,i} t_{\text{sample}}}{(C_{1,i} + C_{2,i}) C_{\text{PD}} I_{\text{source},i} T_{\text{RO}}}\right) + \frac{C_{1,i}^{2} I_{\text{PH},i} t_{\text{sample}}}{(C_{1,i} + C_{2,i}) C_{\text{PD}} I_{\text{source},i} T_{\text{RO}}}$$

$$= N_{i,\text{CM}} \cdot f(T) + \frac{C_{1,i}^{2} t_{\text{sample}}}{(C_{1,i} + C_{2,i}) C_{\text{PD}} I_{\text{source},i} T_{\text{RO}}} I_{\text{PH},i}$$

$$= N_{i,\text{CM}} \cdot f(T) + S_{i} \frac{1}{T_{\text{RO}}} \cdot I_{\text{PH},i}. \tag{9}$$

Resolution values for each channel are measured and verified through electrical [31] and optical measurements. The resolution can be expressed in terms of S_i , as shown in (10), for a sensing channel

$$\begin{aligned} \text{Resolution}_{i} &= \frac{I_{\text{PH},i}^{(2)} - I_{\text{PH},i}^{(1)}}{\left(N_{i}^{(2)} - N_{i}^{(1)}\right) T_{\text{RO}}} \\ &= \frac{I_{\text{PH},i}^{(2)} - I_{\text{PH},i}^{(1)}}{\left(N_{i,\text{CM}} + S_{i} \frac{1}{T_{\text{RO}}} I_{\text{PH},i}^{(2)} - N_{i,\text{CM}} - S_{i} \frac{1}{T_{\text{RO}}} I_{\text{PH},i}^{(1)}\right) T_{\text{RO}}} \\ &= \frac{1}{S_{i}}. \end{aligned} \tag{10}$$

The reference channel has no luminescing cells throughout all the cycles ($I_{PH,r} = 0$ fA); hence, the number of output counts of the reference channel is given by

$$N_{r} = \left(\frac{C_{1,r}^{2} V_{\text{CM},r} + C_{1,r}^{2} I_{D,r} t_{\text{sample}} / C_{\text{PD}}}{(C_{1,r} + C_{2,r}) T_{\text{RO}} I_{\text{source},r}} + \frac{\text{VDDLz} \cdot C_{1,r} C_{2,r} - V_{\text{trip},r} (C_{1,r} + C_{2,r}) C_{1,r}}{(C_{1,r} + C_{2,r}) T_{\text{RO}} I_{\text{source},r}}\right)$$

$$= N_{r,\text{CM}} \cdot f(T). \tag{11}$$

To calibrate the offset variation among each channel throughout cycles, the counts from each sensor channel are first compared to the reference channel by calculating a relative signal R_i

$$R_{i} = \frac{\frac{1}{N_{r}} - \frac{1}{N_{i}}}{\frac{1}{N_{i}}} = \left(\frac{N_{i,\text{CM}} \cdot f(T)}{N_{\text{rCM}} \cdot f(T)} - 1\right) + \frac{S_{i} \cdot I_{\text{PH},i}}{T_{\text{RO}} \cdot N_{r,\text{CM}} \cdot f(T)}$$

$$= (R'_{i,\text{os}} - 1) + \frac{S_{i} \cdot I_{\text{PH},i}}{T_{\text{RO}} \cdot N_{r,\text{CM}} \cdot f(T)}$$

$$= R_{i,\text{os}} + \frac{S_{i} \cdot I_{\text{PH},i}}{T_{\text{RO}} N_{r,\text{CM}} \cdot f(T)}.$$
(12)

 $R'_{i,os}$ is ideally equal to 1 without any channel variation when temperature dependence is canceled for an individual cycle. In practice, $R'_{i,os}$ is ranging from 0.86 to 0.995. For the optical measurements, the first 100 samples, when the LED bias voltage is 0 V, were used to estimate $R'_{i,os}$ of each sensing channel. For the *in vitro* biological measurements, the first 10–30 min were used to estimate $R'_{i,os}$, given that the intestinal inflammation biomarkers require some time to bind with the biosensors. Once $R'_{i,os}$ is obtained, in subsequent measurements, a calibrated number of counts due to luminescence shining on the sensing channel are calculated as

$$\Delta N_{i} = S_{i} \cdot \frac{1}{T_{\text{RO}}} \cdot \Delta I_{\text{PH},i}$$

$$= (R_{i} - R_{i,\text{os}})[N_{r,\text{CM}} \cdot f(T)]$$

$$= N_{i} - R'_{i,\text{os}} \cdot N_{r}. \tag{13}$$

Finally, we obtain the final expression for the estimated photocurrent in terms of measured quantities as given by

$$\Delta I_{\text{PH},i} = \frac{\Delta N_i \cdot T_{\text{RO}}}{S_i} = \Delta N_i \cdot T_{\text{RO}} \cdot \text{Resolution}_i$$
$$= (N_i - R'_{i,\text{os}} \cdot N_r) \cdot T_{\text{RO}} \cdot \text{Resolution}_i. \tag{14}$$

This calibration procedure is performed using MATLAB software (R2021a, The Mathworks, Inc.).

ACKNOWLEDGMENT

The authors would like to thank MUSE Semiconductor for their support in chip fabrication through TSMC and Arun Paidimarri for discussions.

REFERENCES

- [1] A. Amir *et al.*, "Correcting for microbial Blooms in fecal samples during room-temperature shipping," *mSystems*, vol. 2, no. 2, Apr. 2017, Art. no. e00199.
- [2] C. Steiger, A. Abramson, P. Nadeau, A. P. Chandrakasan, R. Langer, and G. Traverso, "Ingestible electronics for diagnostics and therapy," *Nature Rev. Mater.*, vol. 4, no. 2, pp. 83–98, Feb. 2019.
- [3] L. A. Beardslee et al., "Ingestible sensors and sensing systems for minimally invasive diagnosis and monitoring: The next frontier in minimally invasive screening," ACS Sensors, vol. 5, no. 4, pp. 891–910, 2020.
- [4] H. O. Diaz Tartera et al., "Validation of SmartPill wireless motility capsule for gastrointestinal transit time: Intra-subject variability, software accuracy and comparison with video capsule endoscopy," Neurogastroenterol. Motility, vol. 29, no. 10, pp. 1–9, 5 2017.
- [5] M. E. Inda, M. Mimee, and T. K. Lu, "Cell-based biosensors for immunology, inflammation, and allergy," *J. Allergy Clin. Immunol.*, vol. 144, no. 3, pp. 645–647, Sep. 2019.
- [6] M. E. Inda and T. K. Lu, "Microbes as biosensors," Annu. Rev. Microbiol., vol. 74, no. 1, pp. 337–359, Sep. 2020.
- [7] A. Ahmed, J. V. Rushworth, N. A. Hirst, and P. A. Millner, "Biosensors for whole-cell bacterial detection," *Clin. Microbiol. Rev.*, vol. 27, no. 3, pp. 631–646, 2014.

- [8] W. Gao *et al.*, "Fully integrated wearable sensor arrays for multiplexed *in situ* perspiration analysis," *Nature*, vol. 529, pp. 509–514, Jan. 2016.
- [9] V. Ruiz-Valdepeñas Montiel, J. R. Sempionatto, S. Campuzano, J. M. Pingarrón, B. Esteban Fernández de Ávila, and J. Wang, "Direct electrochemical biosensing in gastrointestinal fluids," *Anal. Bioanal. Chem.*, vol. 411, no. 19, pp. 4597–4604, Jul. 2019.
- [10] N. Ostrov et al., "A modular yeast biosensor for low-cost pointof-care pathogen detection," Sci. Adv., vol. 3, no. 6, Jun. 2017, Art. no. e1603221.
- [11] P. Banerjee and A. K. Bhunia, "Cell-based biosensor for rapid screening of pathogens and toxins," *Biosensors Bioelectron.*, vol. 26, no. 1, pp. 99–106, Sep. 2010.
- [12] X. Wan, F. Volpetti, E. Petrova, C. French, S. J. Maerkl, and B. Wang, "Cascaded amplifying circuits enable ultrasensitive cellular sensors for toxic metals," *Nature Chem. Biol.*, vol. 15, no. 5, pp. 540–548, May 2019
- [13] M. O. Din, A. Martin, I. Razinkov, N. Csicsery, and J. Hasty, "Interfacing gene circuits with microelectronics through engineered population dynamics," *Sci. Adv.*, vol. 6, no. 21, May 2020.
- [14] B. Tian et al., "Roadmap on semiconductor-cell biointerfaces," Phys. Biol., vol. 15, no. 3, Mar. 2018, Art. no. 031002.
- [15] P. Kassal, M. D. Steinberg, and I. M. Steinberg, "Wireless chemical sensors and biosensors: A review," Sens. Actuators B, Chem., vol. 266, pp. 228–245, Aug. 2018.
- [16] E. Katz and I. Willner, "Biomolecule-functionalized carbon nanotubes: Applications in nanobioelectronics," *ChemPhysChem*, vol. 5, no. 8, pp. 1084–1104, Aug. 2004.
- [17] S. F. Clarke and J. R. Foster, "A history of blood glucose meters and their role in self-monitoring of diabetes mellitus," *Brit. J. Biomed. Sci.*, vol. 69, no. 2, pp. 83–93, Jan. 2012.
- [18] L. J. Bird et al., "Engineering wired life: Synthetic biology for electroactive bacteria," ACS Synth. Biol., vol. 10, no. 11, pp. 2808–2823, Nov. 2021.
- [19] M.-H. Joe et al., "Pigment-based whole-cell biosensor system for cadmium detection using genetically engineered deinococcus radiodurans," Bioprocess Biosyst. Eng., vol. 35, nos. 1–2, pp. 265–272, Jan. 2012.
- [20] L. Hong, H. Li, H. Yang, and K. Sengupta, "Fully integrated fluorescence biosensors on-chip employing multi-functional nanoplasmonic optical structures in CMOS," *IEEE J. Solid-State Circuits*, vol. 52, no. 9, pp. 2388–2406, Sep. 2017.
- [21] C. Zhu, L. Hong, H. Yang, and K. Sengupta, "Ingestible bioelectronics: A packaged, bio-molecular, fluorescence-based sensor array with ultralow-power wireless interface," in *IEEE MTT-S Int. Microw. Symp. Dig.*, Jun. 2019, pp. 212–215.
- [22] C. Zhu, Y. Wen, T. Liu, H. Yang, and K. Sengupta, "A packaged ingestible bio-pill with 15-pixel multiplexed fluorescence nucleic-acid sensor and bi-directional wireless interface for *in-vivo* bio-molecular sensing," in *Proc. IEEE Symp. VLSI Circuits*, Jun. 2020, pp. 1–2.
- [23] C. Gregor, K. C. Gwosch, S. J. Sahl, and S. W. Hell, "Strongly enhanced bacterial bioluminescence with the ilux operon for single-cell imaging," *Proc. Nat. Acad. Sci. USA*, vol. 115, no. 5, pp. 962–967, Jan. 2018.
- [24] Q. Lin et al., "A 196μW, reconfigurable light-to-digital converter with 119 dB dynamic range, for wearable PPG/NIRS sensors," in Proc. Symp. VLSI Circuits, Jun. 2019, pp. C58–C59.
- [25] H. G. Kim and D. W. Jee, "A <25 μW CMOS monolithic photoplethysmographic sensor with distributed 1b delta-sigma light-to-digital convertor," in *Proc. 43rd IEEE Eur. Solid State Circuits Conf. (ESSCIRC)*, Sep. 2017, pp. 55–58.
- [26] E. K. Bolton, G. S. Sayler, D. E. Nivens, J. M. Rochelle, S. Ripp, and M. L. Simpson, "Integrated CMOS photodetectors and signal processing for very low-level chemical sensing with the bioluminescent bioreporter integrated circuit," *Sens. Actuators B, Chem.*, vol. 85, nos. 1–2, pp. 179–185, 2002.
- [27] S. K. Islam et al., "Integrated circuit biosensors using living whole-cell bioreporters," *IEEE Trans. Circuits Syst. I, Reg. Papers*, vol. 54, no. 1, pp. 89–98, Jan. 2007.
- [28] T. Chi et al., "A multi-modality CMOS sensor array for cell-based assay and drug screening," *IEEE Trans. Biomed. Circuits Syst.*, vol. 9, no. 6, pp. 801–814, Dec. 2015.
- [29] P. Nadeau, M. Mimee, S. Carim, T. K. Lu, and A. P. Chandrakasan, "21.1 nanowatt circuit interface to whole-cell bacterial sensors," in *IEEE Int. Solid-State Circuits Conf. (ISSCC) Dig. Tech. Papers*, Feb. 2017, pp. 352–353.
- [30] M. Mimee et al., "An ingestible bacterial-electronic system to monitor gastrointestinal health," Science, vol. 360, no. 6391, pp. 915–918, May 2018.

- [31] Q. Liu et al., "Zero-crossing-based bio-engineered sensor," in Proc. IEEE Custom Integr. Circuits Conf. (CICC), Apr. 2021, pp. 1–2.
- [32] M. E. Inda et al., "Ingestible capsule for detecting labile inflammatory biomarkers in situ," bioRxiv, to be published, doi: 10.1101/2022.02.16.480562.
- [33] P. Nadeau et al., "Prolonged energy harvesting for ingestible devices," Nature Biomed. Eng., vol. 1, no. 3, Mar. 2017.
- Nature Biomed. Eng., vol. 1, no. 3, Mar. 2017.
 [34] A. F. Yeknami et al., "A 0.3-V CMOS biofuel-cell-powered wireless glucose/lactate biosensing system," IEEE J. Solid-State Circuits, vol. 53, no. 11, pp. 3126–3139, Nov. 2018.
- [35] H. Chen et al., "In situ engineering of intracellular hemoglobin for implantable high-performance biofuel cells," Angew. Chem.-Int. Ed., vol. 58, no. 20, pp. 6663–6668, May 2019.
- [36] K. Kalantar-Zadeh *et al.*, "A human pilot trial of ingestible electronic capsules capable of sensing different gases in the gut," *Nature Electron.*, vol. 1, no. 1, pp. 79–87, Jan. 2018.
- [37] P. M. Nadeau, A. Paidimarri, and A. P. Chandrakasan, "Ultra low-energy relaxation oscillator with 230 fj/cycle efficiency," *IEEE J. Solid-State Circuits*, vol. 51, no. 4, pp. 789–799, Apr. 2016.
- [38] H. Wang and P. P. Mercier, "A reference-free capacitive-discharging oscillator architecture consuming 44.4 pW/75.6 nW at 2.8 Hz/6.4 kHz," *IEEE J. Solid-State Circuits*, vol. 51, no. 6, pp. 1423–1435, Jun. 2016.
- [39] G. Koklu, R. Etienne-Cummings, Y. Leblebici, G. De Micheli, and S. Carrara, "Characterization of standard CMOS compatible photodiodes and pixels for lab-on-chip devices," in *Proc. IEEE Int. Symp. Circuits* Syst. (ISCAS), May 2013, pp. 1075–1078.
- [40] S. B. Alexander, Optical Communication Receiver Design. Bellingham, WA, USA: SPIE, 1997.
- [41] H. Tian, B. Fowler, and A. El Gamal, "Analysis of temporal noise in CMOS photodiode active pixel sensor," *IEEE J. Solid-State Circuits*, vol. 36, no. 1, pp. 92–101, Jan. 2001.
- [42] S. L. Chuang, Physics of Photonic Devices. Hoboken, NJ, USA: Wiley, 2009.
- [43] R. Hui, "Photodetectors," in *Introduction to Fiber-Optic Communications*. Amsterdam, The Netherlands: Elsevier, 2020, pp. 125–154.
- [44] L. Brooks and H.-S. Lee, "A zero-crossing-based 8-bit 200 MS/s pipelined ADC," *IEEE J. Solid-State Circuits*, vol. 42, no. 12, pp. 2677–2687, Dec. 2007.
- [45] L. Brooks and H.-S. Lee, "A 12b 50 MS/s fully differential zero-crossing-based ADC without CMFB," in *IEEE Int. Solid-State Circuits Conf. (ISSCC) Dig. Tech. Papers*, Feb. 2009, pp. 166–167.
- [46] S. Lee, A. P. Chandrakasan, and H.-S. Lee, "A 12b 5-to-50 MS/s 0.5-to-1 V voltage scalable zero-crossing based pipelined ADC," in *Proc. ESSCIRC*, Sep. 2011, pp. 355–358.
- [47] M. Seok, G. Kim, D. Blaauw, and D. Sylvester, "A portable 2-transistor picowatt temperature-compensated voltage reference operating at 0.5 V," *IEEE J. Solid-State Circuits*, vol. 47, no. 10, pp. 2534–2545, Oct. 2012.
- [48] B. Razavi, "The StrongARM Latch," IEEE Solid-State Circuits Mag., vol. 7, no. 2, pp. 12–17, Jun. 2015.
- [49] I. Lee, D. Sylvester, and D. Blaauw, "A constant energy-per-cycle ring oscillator over a wide frequency range for wireless sensor nodes," *IEEE J. Solid-State Circuits*, vol. 51, no. 3, pp. 697–711, Mar. 2016.
- [50] K. Wang, Y. Cao, C.-H. Chang, and X. Ji, "High-speed true random number generator based on differential current starved ring oscillators with improved thermal stability," in *Proc. IEEE Int. Symp. Circuits Syst.* (ISCAS), May 2019, pp. 1–5.
- [51] G. Giustolisi, G. Palumbo, M. Criscione, and F. Cutri, "A low-voltage low-power voltage reference based on subthreshold MOSFETs," *IEEE J. Solid-State Circuits*, vol. 38, no. 1, pp. 151–154, Jan. 2003.
- [52] M. Song et al., "A 3.5 mm×3.8 mm crystal-less MICS transceiver featuring coverages of ±160ppm carrier frequency offset and 4.8-VSWR antenna impedance for insertable smart pills," in *IEEE Int. Solid-State Circuits Conf. (ISSCC) Dig. Tech. Papers*, Feb. 2020, pp. 474–476.



Qijun Liu (Graduate Student Member, IEEE) received the B.Sc. degree in electrical and computer systems engineering from the Rensselaer Polytechnic Institute, Troy, NY, USA, in December 2016. She is currently pursuing the Ph.D. degree with the Department of Electrical and Computer Engineering, Boston University, Boston, MA, USA.

Since the fall of 2018, she has been a Group Member of the Wireless Integrated Systems and Extreme Circuits Laboratory, Boston University, led by Prof. Rabia Tugce Yazicigil. Her research inter-

ests focus on ultra-low-power analog and RF circuit design for biomedical applications.

Ms. Liu received the 2019 International Microwave Symposium (IMS) and Radio Frequency Integrated Circuits Symposium (RFIC) Ph.D. Student Sponsorship and awarded first place in the IMS 2019 Graduate Student Challenge. She is also one of the ISSCC 2020 Student Travel Grant recipients. Her previous work has been accepted by the IEEE Custom Integrated Circuits Conference (CICC) and International Solid-State Circuits Conference (ISSCC) Student Research Preview in 2021.



Miguel Jimenez (Member, IEEE) received the B.A. degree in chemistry and chemical biology from Harvard University, Cambridge, MA, USA, in 2011, and the Ph.D. degree in chemistry from Columbia University, New York, NY, USA, in 2017.

He was a Post-Doctoral Researcher in the group of Robert Langer at the Koch Institute of Integrative Cancer Medicine, Massachusetts Institute of Technology (MIT), Cambridge, MA, USA, from 2017 to 2021. He is currently a Research Scientist in the group of Giovanni Traverso at the

Department of Mechanical Engineering, MIT. His research interests include drug delivery systems for microbial therapeutics, bacterial-electronic devices, and technology for low-resource settings.

Dr. Jimenez is a fellow of the Academy of Bioastronautics at the Translational Research Institute for Space Health (TRISH). He was a recipient of several awards, including the Herchel Smith Undergraduate Fellowship and the National Science Foundation Graduate Fellowship.



Maria Eugenia Inda is currently a Pew Post-Doctoral Fellow with the Synthetic Biology Center, Massachusetts Institute of Technology (MIT), Cambridge, MA, USA. She is building biosensors to diagnose and treat inflammatory disorders in the gut, such as inflammatory bowel disease and celiac disease. Specifically, she is equipping the bacteria dwelling in the intestines with sensors to recognize the molecular markers of inflammation and command them as sentinels to patrol the gut and secrete therapeutic molecules

in situ. In 2019, she started and leads the MIT Microbiome Journal Club with the support of the Center for Microbiome Informatics and Therapeutics (CMIT), MIT/Massachusetts General Hospital (MGH), Boston, MA, USA. Besides, she is thrilled to serve as an MIT-Comm Lab Advisor using her prowess to help students show the value of their ideas and push their scientific career forward.

Dr. Inda is also the 2020 Langer Fellow for Innovation and Entrepreneurial Excellence—American Institute of Chemical Engineers (AIChE). She was a Topic Editor of *Biosensors* (MDPI) in 2020 and an MIT IMPACT Fellow in 2017.



Arslan Riaz (Graduate Student Member, IEEE) received the B.S. degree in electrical engineering from the National University of Sciences and Technology (NUST), Islamabad, Pakistan, in 2018. He is currently pursuing the Ph.D. degree with the Electrical and Computer Engineering Department (ECE), Boston University, Boston, MA, USA.

His Ph.D. research is oriented toward developing energy-efficient and secure wireless communication systems. He was a Research Assistant with the Electrical Engineering Department, Lahore University of

Management Sciences (LUMS), Lahore, Pakistan, from 2018 to 2019. He is currently a member of the Wireless Integrated Systems and Extreme Circuits Laboratory, Boston University. His research was focused on RF circuit design and energy harvesting for the Internet of Things (IoTs).



Timur Zirtiloglu (Graduate Student Member, IEEE) received the B.Sc. degree in electronics engineering from Sabanci University, Istanbul, Turkey, in 2019. He is currently pursuing the Ph.D. degree with the Department of Electrical and Computer Engineering, Boston University, Boston, MA, USA.

He is currently a Group Member of the Wireless Integrated Systems and Extreme Circuits Laboratory (WISE-Circuits), Boston University. His recent work has been published at the IEEE Custom Integrated Circuits Conference (CICC) in 2021. His research

interests focus on a joint design of advanced analog and RF circuit techniques with novel signal processing algorithms for communication systems. He is also interested in the design of ultra-low-power circuits for biomedical applications.

Mr. Zirtiloglu received the 2019 IMS and RFIC NSF Student Conference Registration Award, the IEEE CICC 2020 Student Education Grant Award, and the IEEE 2022 Solid-State Circuits Society Student Travel Grant Award (SGTA).



Anantha P. Chandrakasan (Fellow, IEEE) received the B.S., M.S., and Ph.D. degrees in electrical engineering and computer sciences from the University of California at Berkeley, Berkeley, CA, USA, in 1989, 1990, and 1994, respectively.

Since September 1994, he has been with the Massachusetts Institute of Technology (MIT), Cambridge, MA, USA, where he is currently the Vannevar Bush Professor of electrical engineering and computer science. He was the Director of the Microsystems Technology Laboratories, MIT,

from 2006 to 2011. From July 2011 to June 2017, he was the Head of the Department of Electrical Engineering and Computer Science, MIT. Since July 2017, he has been the Dean of the School of Engineering, MIT. He is a coauthor of Low Power Digital CMOS Design (Kluwer Academic Publishers, 1995), Digital Integrated Circuits (Pearson Prentice-Hall, second edition, 2003), and Sub-Threshold Design for Ultra Low-Power Systems (Springer 2006). His research interests include ultra-low-power circuit and system design, energy harvesting, energy-efficient RF circuits, and hardware security.

Dr. Chandrakasan was elected as a fellow of the Association for Computing Machinery (ACM) in 2020. He was a co-recipient of several awards, including the 2007 ISSCC Beatrice Winner Award for Editorial Excellence and the ISSCC Jack Kilby Award for Outstanding Student Paper in 2007, 2008, and 2009. He received the 2009 Semiconductor Industry Association (SIA) University Researcher Award and the 2013 IEEE Donald O. Pederson Award in Solid-State Circuits, an honorary doctorate from KU Leuven in 2016, the UC Berkelev EE Distinguished Alumni Award in 2017, and the 2019 IEEE Solid-State Circuits Society Distinguished Service Award. In 2015, he was elected to the National Academy of Engineering. In 2019, he was elected to the American Academy of Arts & Sciences. He has served in various roles in the IEEE International Solid-State Circuits Conference (ISSCC), including the Program Chair, the Signal Processing Sub-Committee Chair, and the Technology Directions Sub-Committee Chair. He has served as the Conference Chair for ISSCC from 2010 to 2018. He also serves as a Senior Technical Advisor to the conference starting ISSCC 2019.



Timothy K. Lu received the B.S. and M.Eng. degrees in electrical engineering and computer science from the Massachusetts Institute of Technology (MIT), Cambridge, MA, USA, in 2003, the Ph.D. degree from MIT in 2007, and the M.D. degree from the Harvard Medical School in 2010.

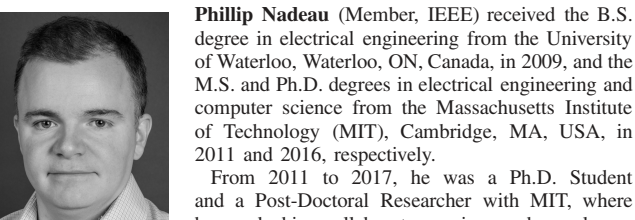
He is currently an Associate Professor with the Department of Biological Engineering and the Department of Electrical Engineering and Computer Science, MIT. He is also a Founding Member of the MIT Synthetic Biology Center, a member of the

MIT Microbiology Program and the MIT Computational Systems Biology Initiative, and an Associate Member of the Broad Institute of MIT and Harvard University, Cambridge.



parameters.

Giovanni Traverso (Member, IEEE) is a gastroenterologist and a biomedical engineer. He is currently an Assistant Professor with the Department of Mechanical Engineering, Massachusetts Institute of Technology, Cambridge, MA, USA, and the Brigham and Women's Hospital, Harvard Medical School, Boston, MA, USA. His current research program is focused on developing the next generation of drug delivery systems to enable safe and efficient delivery of therapeutics through the gastrointestinal tract and developing novel ingestible electronic devices for sensing a broad array of physiologic and pathophysiologic



From 2011 to 2017, he was a Ph.D. Student and a Post-Doctoral Researcher with MIT, where he and his collaborators pioneered work on bacterial-electronic biosensors in wireless capsules

for the gastrointestinal tract. He previously held internships at Texas İnstrument's Kilby Labs, Dallas, TX, USA, in 2012 and 2014, and Intel's Radio Integration Lab, Hillsboro, OR, USA, in 2011. In 2017, he joined Analog Devices Inc., Boston, MA, USA, where he is currently a Senior Research Scientist managing research and development activities for novel bioelectronic platforms, including DNA sequencing, DNA synthesis, and single-cell biology. He has also conducted research on circuits and algorithms for analog computein-memory (CiM) systems, battery-less wireless temperature sensors, and wireless indoor positioning systems.

Dr. Nadeau also serves as a TPC Member of the VLSI Symposium and a Committee Member of the Student Research Preview at IEEE International Solid-State Circuits Conference (ISSCC). His awards include the Qualcomm Innovation Fellowship in 2014, the MIT Harold Hazen Teaching Award in 2012, and the Governor General of Canada's Academic Medal in 2009.



Rabia Tugce Yazicigil (Member, IEEE) received the B.S. degree in electronics engineering from Sabanci University, Istanbul, Turkey, in 2009, the M.S. degree in electrical and electronics engineering from the École Polytechnique Fédérale de Lausanne (EPFL), Lausanne, Switzerland, in 2011, and the Ph.D. degree in electrical engineering from Columbia University, New York, NY, USA, in 2016.

She was a Post-Doctoral Research Associate with the Department of Electrical Engineering and Computer Science, Massachusetts Institute of Technology

(MIT), Cambridge, MA, USA, from 2016 to 2018. She is currently an Assistant Professor with the Electrical and Computer Engineering Department, Boston University, Boston, MA, USA. Her research interests lie at the interface of integrated circuits, bio-sensing, signal processing, security, and wireless communications to innovate system-level solutions for future energyconstrained applications.

Dr. Yazicigil is also a member of the 2015 MIT EECS Rising Stars Cohort. She was a recipient of a number of awards, including the Electrical Engineering Collaborative Research Award for her Ph.D. research on compressive sampling applications in rapid RF spectrum sensing in 2016, the Second Place at the Bell Labs Future X Days Student Research Competition in 2015, the Analog Devices Inc. Outstanding Student Designer Award in 2015, and the 2014 Millman Teaching Assistant Award of Columbia University. She has served as the Vice-Chair of the Rising Stars 2020 Workshop at the IEEE International Solid-State Circuits Conference (ISSCC). She also serves on the Technical Program Committee (TPC) of IEEE ISSCC and TPC of IEEE European Solid-State Circuits Conference (ESSCIRC).